Spatial and temporal wave climate variability along the south coast of Sweden during 1959–2021

Adell, Anna; Almström, Björn; Kroon, Aart; Larson, Magnus; Uvo, Cintia Bertacchi; Hallin, Caroline

DOI
10.1016/j.rsma.2023.103011

Publication date
2023

Document Version
Final published version

Published in
Regional Studies in Marine Science

Citation (APA)
Adell, A., Almström, B., Kroon, A., Larson, M., Uvo, C. B., & Hallin, C. (2023). Spatial and temporal wave climate variability along the south coast of Sweden during 1959–2021. *Regional Studies in Marine Science*, *63*, Article 103011. https://doi.org/10.1016/j.rsma.2023.103011

Regional Studies in Marine Science 63 (2023) 103011

Contents lists available at ScienceDirect

Regional Studies in Marine Science

journal homepage: www.elsevier.com/locate/rsma

Spatial and temporal wave climate variability along the south coast of Sweden during 1959–2021

Anna Adell [a,b,*], Björn Almström [a], Aart Kroon [b], Magnus Larson [a], Cintia Bertacchi Uvo [a,c], Caroline Hallin [a,d]

[a] Department of Water Resources Engineering, Lund University, Box 118 SE-221 00 Lund, Sweden
[b] Department of Geosciences and Natural Resource Management, University of Copenhagen, Copenhagen, Denmark
[c] Finnish Environment Institute, Helsinki, Finland
[d] Department of Hydraulic Engineering, Delft University of Technology, Delft, The Netherlands

ARTICLE INFO

Article history:
Received 29 March 2023
Received in revised form 4 May 2023
Accepted 15 May 2023
Available online 19 May 2023

Keywords:
Wave hindcast
south Baltic Sea
SWAN
NAO

ABSTRACT

This study presents 62 years of hindcast wave climate data for the south coast of Sweden from 1959–2021. The 100-km-long coast consists mainly of sandy beaches and eroding bluffs interrupted by headlands and harbours alongshore, making it sensitive to variations in incoming wave direction. A SWAN wave model of the Baltic Sea, extending from the North Sea to the Åland Sea, was calibrated and validated against wave observations from 16 locations distributed within the model domain. Wave data collected from open databases were complemented with new wave buoy observations from two nearshore locations within the study area at 14 and 15 m depth. The simulated significant wave height showed good agreement with the local observations, with an average R^2 of 0.83. The multi-decadal hindcast data was used to analyse spatial and temporal wave climate variability. The results show that the directional distribution of incoming waves varies along the coast, with a gradually increasing wave energy exposure from the west towards the east. The wave climate is most energetic from October to March, with the highest wave heights in November, December, and January. In general, waves from westerly directions dominate the annual wave energy, but within the hindcast time series, a few years had larger wave energy from easterly directions. The interannual variability of total wave energy and wave direction is correlated to the North Atlantic Oscillation (NAO) index. In the offshore, the total annual wave energy had a statistically significant positive correlation with the NAO DJFM station-based index, with a Spearman rank correlation coefficient of 0.51. In the nearshore, the correlation was even stronger. Future studies should investigate the possibility of using the NAO index as a proxy for the wave energy direction and its effect on coastal evolution.

1. Introduction

Coastal areas worldwide are threatened by flooding and erosion, problems which are expected to be aggravated due to rising sea levels (Luijendijk et al., 2018; Nicholls, 2002; Oppenheimer et al., 2019; Wong et al., 2014). Mitigating these increased risks requires effective coastal management and planning strategies (Lincke and Hinkel, 2018); these rely on knowledge and understanding of the local wave climate conditions. Wind-generated waves account for the main energy input to the nearshore and drive littoral processes (Davidson-Arnott, 2010; Huntley, 2013). However, wave observations are generally scarce, and the length of data records is often limited compared to the design and planning lifetimes of coastal infrastructure (Van der Meer et al., 2018). Instead, numerical models are commonly used to generate hindcasts and forecasts of wave climate parameters across multiple temporal and spatial scales.

This study focuses on the south coast of Sweden, which has a relatively high population density and abundant critical near-coastal infrastructure but scarce information about the wave climate conditions. The coast is located in the south Baltic Sea and is oriented in an east–west direction (Fig. 1). The low-lying landscape and predominance of sandy beaches make it subject to the risk of coastal flooding and erosion (Larson and Hanson, 1993). The coast mainly consists of sandy beaches and eroding bluffs, interrupted by headlands, harbours, and hard coastal protection. The geological setting and man-made structures along the coast make the coastal evolution sensitive to changes in the prevailing wave energy direction (Larson et al., 2016).

The wave climate in the Baltic Sea is dominated by short-period wind-generated waves. The semi-enclosed sea measures

* Corresponding author at: Department of Water Resources Engineering, Lund University, Box 118 SE-221 00 Lund, Sweden.
E-mail address: anna.adell@tvrl.lth.se (A. Adell).

https://doi.org/10.1016/j.rsma.2023.103011

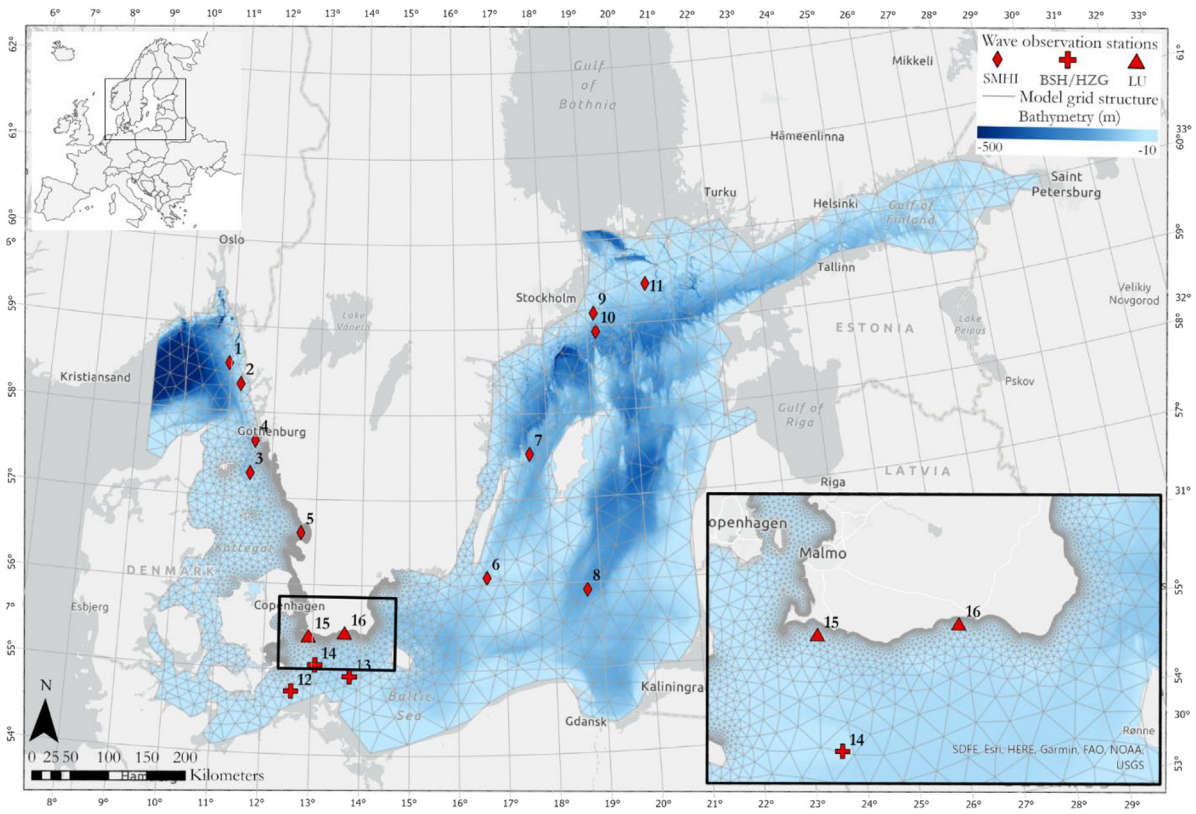

Fig. 1. Map showing the study area and model domain with the grid structure, including the locations of wave gauges operated by SMHI, BSH/HZG, and LU.

392,978 km^2 (Leppäranta and Myrberg, 2009), and the narrow straits connecting the Baltic Sea to the North Sea eliminate swell waves from propagating into the basin. The waves reaching the south coast of Sweden are generated within the Arkona Basin in the southwest part of the Baltic Sea. The Arkona Basin, bordered by Sweden in the north and Germany in the south, is one of the shallowest parts of the Baltic Sea, with a mean depth of 23 m and a maximum depth of 53 m (Rosentau et al., 2017). The geographical setting enables spatial and temporal variations in the Baltic Sea wave climate to arise due to even slight changes in wind direction (Broman et al., 2006; Soomere and Räämet, 2011).

Wind climatic conditions over the Baltic Sea region are governed by atmospheric teleconnection patterns of the Northern Hemisphere and European-Atlantic sectors (Bierstedt et al., 2015; Hurrell, 1995; Hurrell et al., 2003; Rutgersson et al., 2014), specially by the North Atlantic Oscillation (NAO), Arctic Oscillation (AO), and Scandinavian pattern (SCAND). Previous studies have correlated water level fluctuations (e.g., Andersson, 2002; Woolf et al., 2003) and extent of sea-ice coverage (Jevrejeva et al., 2003; Omstedt and Chen, 2001) in the Baltic Sea basin to the NAO and AO. However, the influence of atmospheric circulation systems on wave climate has not been studied to the same extent (Najafzadeh et al., 2021). A study conducted by Najafzadeh et al. (2021) found a statistically significant correlation between Baltic Sea winter season wave climate and the three mentioned circulation patterns as represented by their indices.

For the wave climate on the Swedish south coast, NAO has shown to be the most relevant to investigate. The NAO index is based on the difference in sea level pressure (SLP) between Lisbon, Portugal, and Stykkisholmur, Iceland (Hurrell, 1995). The positive phase of the NAO is associated with stronger than normal westerly winds towards northern Europe during winter time. In the negative phase, the westerly winds are weaker than normal over northern Europe, that facilitates the occurrence of easterly winds (Hurrell, 1995). The variability of the distribution of westerly and easterly winds are expected to influence the local wave climate and the morphological evolution of the east–west oriented coastline of south Sweden.

The wave climate in the Baltic Sea has previously been hindcasted and analysed over a range of spatial and temporal scales (e.g., Björkqvist et al., 2018; Blomgren et al., 2001; Jönsson et al., 2003; Soomere et al., 2012). Jönsson et al. (2003) simulated one year of wave data for the entire Baltic Sea basin with the HYPAS model; Blomgren et al. (2001) presented a 19-year hindcast for the southern Baltic Sea, simulated with the WAVAD model; and Björkqvist et al. (2018) computed wave statistics based on wave hindcast data from 1965–2005 simulated in SWAN for the whole Baltic Sea with a 6-hour temporal resolution and with a spatial resolution of 1.85 × 3.7 km. Soomere et al. (2012) analysed simulated and observed wave climate data specifically for the Arkona Basin to present typical wave conditions and features of the wave climate. Additional studies have utilized knowledge of historical regional wave climate simulations to compile projections for future wave climate conditions adopting different RCP scenarios (Bonaduce et al., 2019; Suursaar et al., 2016). Still, a comprehensive study of the nearshore wave climate does not exist for the south coast of Sweden.

This study aims to (i) characterize the wave climate conditions along the south coast of Sweden and (ii) investigate the interannual wave climate variability and how it relates to the NAO. In this study, the wave climate for the south coast of Sweden is derived through numerical modelling in SWAN (Booij et al., 1999), and hindcast wave climate conditions are presented from 1959–2021. The model is validated across offshore and nearshore model domains represented by observations at 16 locations, available through public databases and new wave buoy measurements. The generated hindcast data provides high-resolution wave climate data over six decades, enabling investigation of decadal, annual and seasonal wave climate variability. The hindcast data are analysed to characterize the spatial and temporal variability in wave

climate conditions along the south coast of Sweden. Interannual variations in the wave energy are analysed in relation to the NAO.

2. Data and methodology

2.1. Wave modelling - SWAN

Numerous wave models of varying levels of complexity are available to simulate wind-generated wave climate. The deep-water characteristics of wave height and wave period can be computed based on the relationship between fetch length, wind speed and duration according to the Sverdrup-Munch-Bretschneider (SMB) formulations (USACE, 1984). This constitutes a simple empirical method widely applied in coastal engineering practices, although of relatively low complexity. More advanced numerical models must be used to account for more complex wave transformation processes like wave refraction and shoaling, energy dissipation, and wave breaking. Models of higher complexity are typically categorized as phase-averaged or phase-resolving models. Phase-averaged models utilize the wave spectrum to determine the wave evolution based on statistically derived wave parameters. In phase-resolving models, the wave phases are computed explicitly for individual waves (Cavaleri et al., 2007). This typically contributes to higher computational demand for phase-resolving models than phase-averaged models, which consequently are more commonly used on a delimited scale for detailed analysis. Phase-averaged models are suitable for the analysis of wave climate on regional scales and annual to decal temporal scales.

In this study, the wave climate was hindcast using the third-generation spectral wave model SWAN (version 41.31), Simulating WAves Nearshore (Booij et al., 1999). The SWAN model can resolve wave climate both in deep water and in the nearshore and is therefore suitable for long-term regional wave climate hindcast modelling that spans multiple spatial scales.

In SWAN, the propagation of wave energy is governed by the spectral action balance equation (Eq. (1)) that describes the evolution of the two-dimensional wave action density spectrum, N (Booij et al., 1999),

$$\frac{\partial N}{\partial t} + \frac{\partial c_x N}{\partial x} + \frac{\partial c_y N}{\partial y} + \frac{\partial c_\sigma N}{\partial \sigma} + \frac{\partial c_\theta N}{\partial \theta} = \frac{S_{tot}}{\sigma} \tag{1}$$

The terms on the left-hand side of the equation describe the kinematics, i.e., propagation of action density in time, propagation of action density in the x- and y-directions, shifting of relative frequencies due to variation in depth and currents, and depth and current induced refraction. The term on the right-hand side of Eq. (1) is the source and sink term for energy density, where S_{tot} represents the processes of generation, dissipation, and redistribution of wave energy:

$$S_{tot} = S_{in} + S_{wc} + S_{nl4} + S_{bot} + S_{brk} + S_{nl3} \tag{2}$$

Deep water processes are represented by S_{in}, S_{wc} and $S_{nl4.}$, where S_{in} is the energy transfer from the wind to the waves, S_{wc} is the dissipation of wave energy due to white capping, and S_{nl4} is the nonlinear transfer of wave energy due to quadruplet interaction. Shallow water processes include S_{bot} which is the energy dissipation due to bottom friction, S_{brk} is the energy loss due to depth-induced breaking, and S_{nl3} relates to nonlinear triad interaction. A more detailed explanation of the formulations of the processes is found in, e.g. Booij et al., 1999; Holthuijsen, 2007.

The model domain covers the southern Baltic Sea, the Sound, Kattegat and Skagerrak with closed boundaries facing the North Sea and the Åland Sea (Fig. 1) and utilizes an unstructured computational mesh, generated using OceanMesh2D (Roberts et al., 2019). Finer resolution is applied in the nearshore to accurately resolve the wave dynamics while a coarser resolution is applied in the offshore to reduce computational time (Zijlema, 2009, 2010). The maximum grid cell resolution in the offshore regions is 25 km, gradually decreasing to 200 m at the coast. The model was run with 36 directional bins and 38 frequency bins equally spaced in the range of 0.03–1 Hz. The timestep of the simulation was 10 min and the temporal resolution of the output was 3 h.

2.2. Input data

The bathymetry interpolated onto the unstructured model grid in the offshore was obtained from EMODnet with a 115 x 115 m resolution (EMODnet, 2021). In the nearshore, from approximately 1 to 10 m depth, a more detailed bathymetry with 2 x 2 m resolution was applied (Malmberg-Persson et al., 2016).

Wind field forcing was obtained from the ERA5 global reanalysis dataset provided by the European Centre for Medium-Range Weather Forecasts (ECMWF) (Hersbach et al., 2020). The reanalysis dataset is derived through data assimilation, i.e., combining sources of model data and observations with global coverage. The spatial resolution of the grid cells for atmospheric quantities is 0.25° x 0.25° (approximately 30 x 30 km). For this study, averaged wind data (u- and v-components) at 10 m elevation were extracted from June 1959 to December 2021, with a 3-hour temporal resolution. The model wind input had a spatial extent of [2.5; 53] to [32; 62] ([longitude; latitude]), which covers the Baltic Sea and part of the North Sea.

Historical values for the NAO index from 1864 to 2022 were obtained from National Centre for Atmospheric Research (NCAR) (NCAR, 2023). The DJFM station-based index was used. The value for year N represents an average for the winter period expanding from December year N-1 to March year N. The correlation between the simulated wave climate and the large-scale atmospheric circulation, NAO, was assessed through Spearman rank correlation analysis.

2.3. Wave observations

2.3.1. Available historical records

Historical wave observation data within the model domain were available open-access from the Swedish Metrological and Hydrological Institute (SMHI) and the Federal Maritime and Hydrographic Agency of Germany (BSH). The distribution of stations is indicated in Fig. 1. The length of operation periods varies between the stations and extend from a few months to several decades. Only stations with at least one year of data were considered in the calibration and validation process.

The open-access SMHI data are recorded with either bottom-mounted echo sonar or surface accelerometer buoys. At stations Trubaduren (4), Ölands södra grund (6) and Almagrundet (9), waves were measured with a bottom-mounted echo sonar equipment installed close to a caisson lighthouse, and data transmission for further processing was facilitated via a cable (Svensson and Wickström, 1986). Measurements at stations using this technique commenced at the end of the 1970s, and the operation continued until the beginning of the 21st century. At stations, Laholmsbukten (5) and Svenska Björn (11) surface accelerometer buoys were installed to measure the wave parameters in shorter campaigns. Since 2005, SMHI use Datawell directional waverider buoys (SMHI, 2022). These are currently installed to measure the waves at stations Väderöarna (1), Brofjorden (2), Knolls grund (7) and Huvudskär Ost (10).

Measurements at the station Darsser Sill (12) commenced in 1991, initiated by Helmholtz Zentrum Geesthacht (HZG). Stations Arkona (13) and FINO2 (14) are operated by BSH. At FINO2, wave parameters were measured using a Datawell sea state buoy

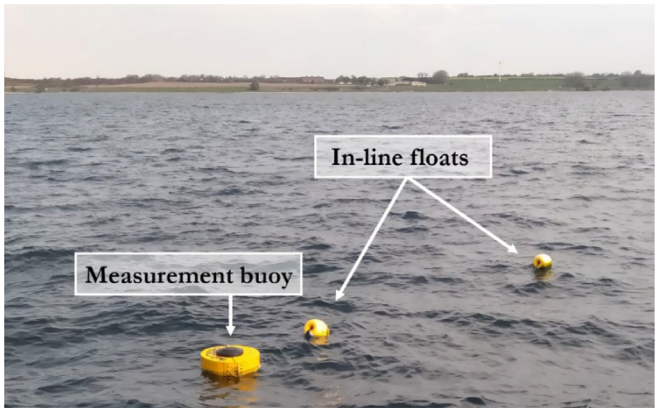

Fig. 2. Obscape WaveDroid directional wave buoy used for data collection of nearshore wave parameters. Buoy housing and in-line floats are visible at the surface. The picture was taken at the location Ystad (16), in May 2021.

with an MKIII sensor (BSH, 2019). At stations Arkona and Darss Sill, surface acceleration buoys Seawatch Directional Waverid-ers were installed to record the observations (Pettersson et al., 2014; Soomere et al., 2012). Data for these stations are available open-access at the Sea states data portal (BSH, 2021).

2.3.2. Nearshore observations

The available wave observations were complemented with additional nearshore wave observations from the study area. Two surface acceleration buoys Obscape WaveDroid Block III (Obscape, n.d.) were deployed from Nov 2020 to May 2021 at stations Kämpinge (15) and Ystad (16) at 15- and 14-meter depths, re-spectively (Fig. 1). Fig. 2 shows the equipment set up at the field site. The measurement buoy was anchored with an anchor weight of 15 kg, connected by a mooring line. The mooring line system had two in-line floats at the surface and an in-line weight of 1.5 kg between them; this design allowed the buoy to move with the wave orbital motion. The water level variation was recorded at a frequency of 5.82 Hz in bursts of 23 min. The filtered frequency range was 0.05 Hz–1.00 Hz. Bulk wave parameters significant wave height (H_s), maximum wave height (H_{max}), peak wave period (T_p), mean wave period (T_{m01}), peak wave direction (θ), and peak directional spreading (σ_p) were processed with a 30-minute resolution. Post-processing of the data included low pass filtering with respect to wave energy. Spectral energy at frequencies below 0.1 Hz was discarded.

2.4. Model calibration and validation

The model was calibrated by compairing simulated results of H_s with corresponding observations during July 2005–June 2009 from stations Väderöarna (1), Södra Östersjön (8), Huvud-skär Ost (10), and Darsser Sill (12). The *Coefficient of Determi-nation* (R^2) and *Root Mean Square Error* (RMSE) were used to evaluate model performance and guide the calibration procedure. In addition, visual comparisons of the simulated and observed time series were conducted to ensure good representation of the timing and magnitude of peaks.

The model was set up with mostly default configurations of SWAN version 41.31 and run in third-generation mode (GEN3). Activated processes include generation by wind, quadruple and triad wave interactions, depth induced wave breaking, dissipation through bottom friction and white capping. The maximum wind drag (cdcap) was set to a suggested value of 2.5e−3 (The SWAN Team, 2020). During the assessment a good fit was prioritized for stations located in the southern Baltic Sea basin, i.e., Södra Östersjön and Darsser Sill, while still considering the overall performance in the adjacent sub-basins in the domain at stations Väderöarna and Huvudskär Ost. The white capping formulations applied were according to Komen et al. (1984). In the calibra-tion procedure, the coefficient for determining the rate of white capping dissipation (cds2) was adjusted from 2.36e−5 (default setting) to 1.10e−5. This gave a better fit for larger wave heights while not compromising the model performance for milder wave conditions.

The model was validated against the remaining H_s observation records from wave gauges distributed in the model domain. In addition, the model has been validated against nearshore wave observations at stations Kämpinge (15) and Ystad (16). At the nearshore stations, data for peak wave period and wave direction are also considered for validation.

3. Results

3.1. Model performance

Re-calibration of the model coefficient to determine rate of white capping dissipation was required to improve model per-formance. Table 1 presents the model performance before and after the calibration procedure for the four stations considered. Occasionally there has been interruptions in the observations leading to non-continuous records, the number of observations presented in Table 1 refers to number of matching data points between observed and simulated datasets during the calibration period. The adjustment of the model configuration on average in-creased R^2 results by 5.5% for the calibration dataset, while RMSE was reduced by an average of 10.9% (Table 1). The alteration of white capping configuration had the most significant effect on the largest wave height in the calibration datasets.

Validation results for all stations operated by SMHI, BSH and HZG are presented in Table 2 and represent an assessment of the model performance in offshore regions of the model domain. Similar to the calibration procedure, measures of R^2 and RMSE for correlation between observed and simulated H_s were considered to assess model performance. The calibration period has been excluded in the validation period for stations 1, 8, 10, an 12. The results indicate that the model performance is good, reflected by average R^2-values of 0.83 $\pm$ 0.08 and RMSE of 0.26 $\pm$ 0.08 m for significant wave height.

Fig. 3 shows scatter plots comparing observed and simulated wave parameters for the nearshore station at Kämpinge (15) and Ystad (16). H_s is well-represented by the model, indicated by the high R^2 values of 0.90 for Ystad and 0.86 for Kämpinge. The time series comparison between observed and simulated H_s presented in Fig. 4 shows that the model can represent the timing of peaks and mostly matches the magnitude of the peaks. However, the peaks for storm wave heights are occasionally underestimated both at stations Kämpinge (15) and Ystad (16). This discrepancy is also noticed in the correlation plots in Fig. 3 (a) and (d), where larger wave heights (approx. 3 m) display more scatter. The model fit for peak period T_p and direction, θ is slightly less accurate, with R^2 values of 0.48 and 0.57 and RMSE of 0.93 for T_p (Fig. 3(b) and (e)). The assessment yields result of R^2 of 0.74 and 0.61 and RMSE of 26.7 and 25.0 for wave direction at stations Kämpinge and Ystad, respectively (Fig. 3(c) and (f)). The more scattered result obtained for T_p and θ is related to low-energy noise of short waves. When filtering the observed records based on wave steepness (H_s/L, where $L = g \cdot T_p^2/2\pi$) and removing waves with steepness below 0.012, the assessment results of the peak variables T_p and θ were improved. At Kämpinge R^2 increased from 0.48 to 0.71 for T_p and from 0.74 to 0.81 for θ. At Ystad R^2 increased from 0.57 to 0.71 for T_p and from 0.61 to 0.80 for θ.

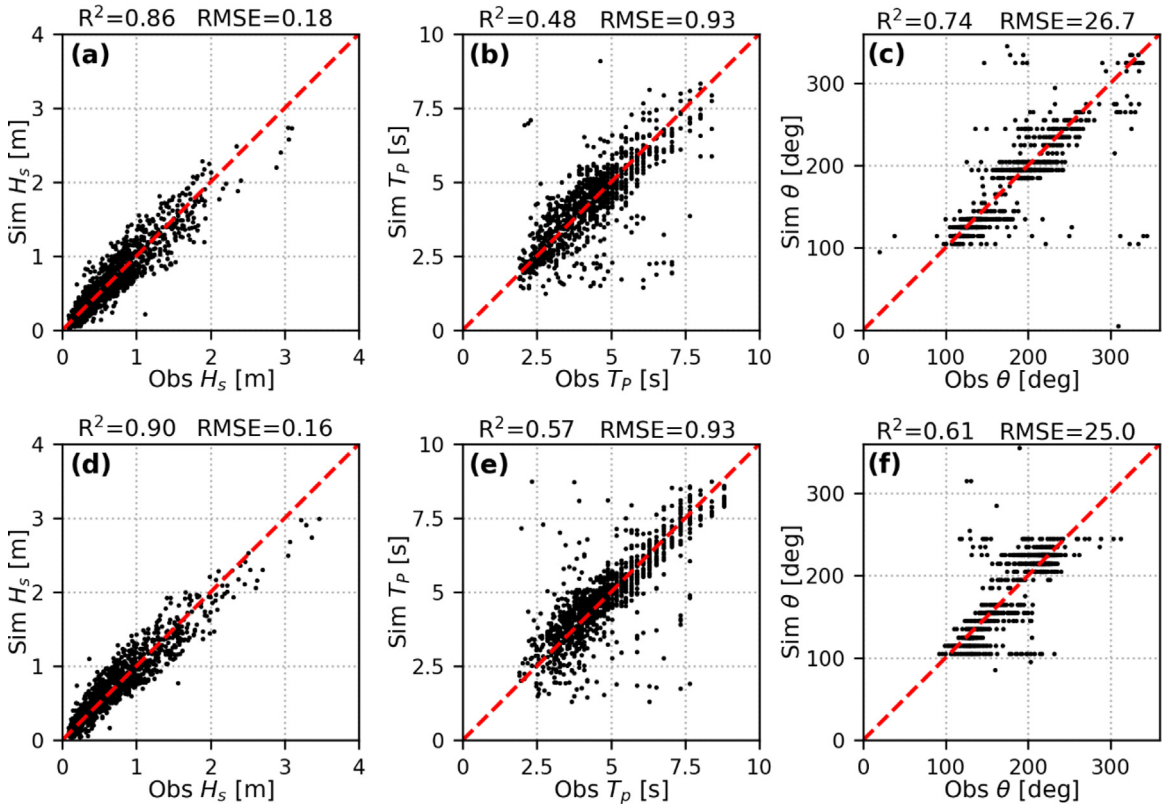

Fig. 3. Validation results to assess model fit for wave climate parameters, H_s, T_p and θ at nearshore station 15-Kämpinge (a-c) and 16-Ystad (d-e). The red dashed line corresponds to a perfect fit.

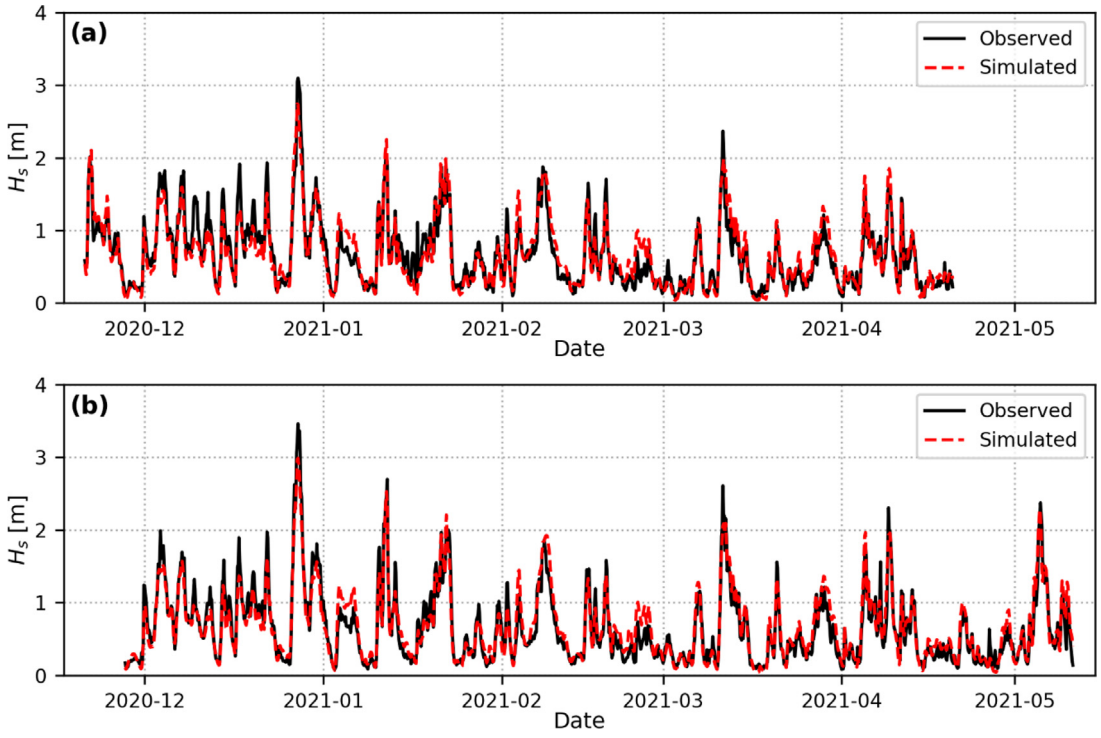

Fig. 4. Time series comparison between observed and simulated H_s at locations 15-Kämpinge (a) and 16-Ystad (b).

Table 1
Model performance, assessed in terms of R^2 and RMSE, before and after the calibration procedure. Number of observations refer to the number of matching data points between the observed and simulated datasets during the calibration period.

Nr.	Station name	Calibration period	No. obs	Before calibration		After calibration	
				R^2	RMSE	R^2	RMSE
1	Väderöarna WR	July 2005–June 2009	10954	0.69	0.50	0.80	0.40
8	Södra Östersjön	Mar 2006–June 2009	6381	0.89	0.29	0.92	0.24
10	Huvudskär Ost	Nov 2005–June 2009	5861	0.89	0.23	0.88	0.24
12	Darsser Sill	July 2005–June 2009	9353	0.84	0.19	0.87	0.17

Table 2
Details of wave observations used for model validation, including station name, validation period, and responsible operator. The station number corresponds to the numbering used in Fig. 1. Coefficient of determination, R^2, and RMSE, obtained from comparison of wave parameters for the overlap between the simulation period (June 1959–December 2021) and each station's operational period.

Nr.	Station name	Validation period	Operator	Parameter	R^2	RMSE
1	Väderöarna WR	July 2009–Dec 2021	SMHI	H_s (m)	0.83	0.36
2	Brofjorden WR	Feb 2017–Dec 2021	SMHI	H_s (m)	0.83	0.33
3	Läsö-Ost	May 2001–Feb 2009	SMHI	H_s (m)	0.75	0.25
4	Trubaduren	Oct 1978–Oct 2003	SMHI	H_s (m)	0.71	0.29
5	Laholmsbukten	Mar 1984–Oct 1985	SMHI	H_s (m)	0.88	0.17
6	Ölands S grund	Oct 1978–Mar 2004	SMHI	H_s (m)	0.83	0.29
7	Knolls grund	Nov 2011–Dec 2021	SMHI	H_s (m)	0.84	0.26
8	Södra Östersjön	July 2009–Apr 2011	SMHI	H_s (m)	0.93	0.24
9	Almagrundet	Oct 1978–Sept 2003	SMHI	H_s (m)	0.58	0.49
10	Huvudskär Ost	May 2001–June 2005 July 2009–Dec 2021	SMHI	H_s (m)	0.87	0.23
11	Svenska Björn	Nov 1982–Nov 1986	SMHI	H_s (m)	0.85	0.30
12	Darsser Sill	Feb 1991–June 2005 July 2009–May 2020	HZG	H_s (m)	0.83	0.20
13	Arkona	June 2013–Dec 2021	BSH	H_s (m)	0.89	0.21
14	FINO2 platform	May 2011–Sept 2020	BSH	H_s (m)	0.88	0.21
15	Kämpinge	Nov 2020–Apr 2021	LU	H_s (m)	0.86	0.18
				T_p (s)	0.48	0.93
				θ (deg.) 0.74	26.7	
16	Ystad	Nov 2020–May 2021	LU	H_s(m)	0.90	0.16
				T_p (s)	0.57	0.93
				θ (deg.)	0.61	25.0

3.2. Spatial wave climate variability

Fig. 5 displays the 95th percentile H_s for the period July 1959-December 2021, where blue colours represent milder wave conditions and red represents more energetic wave conditions. The result shows that the wave climate is more energetic in the east part of the study area compared to the west. The spatial pattern also visualizes the sheltering effects of the confined embayments along the south coast of Sweden, and similarly, the sheltering effects of the island of Bornholm in the east.

The upper panels in Fig. 5 show the variability in local wave climate conditions along the south coast of Sweden (wave roses at locations *a*-*e*). The directional distribution of incoming waves differs between the locations due to the varying exposure and shoreline orientations. The 95th percentile H_s for the five locations are 1.34 m (*a.*; Kämpinge), 1.59 m (*b.*; Smygehamn), 1.46 m (*c.*; Svarte), 1.89 m (*d.*; Sandhammaren), and 2.28 m (*e.*; Sydkusten). The greater wave heights converge towards the headland locations (*b* and *d*), whereas the embayed locations (*a* and *c*) display slightly lower wave heights, this highlights the influence of the complex appearance of the coastline of south Sweden. Furthermore, the frequency of occurrence of greater wave heights progressively increases towards the east. This is caused by varying fetch lengths that serve the different locations. Fig. 5e represents a location to exemplify the generic open ocean conditions, for a point exposed to waves in all directions. The results show that waves in the sectors west, west-southwest, and southwest dominate, followed by north-northeast and east. Fig. 6 presents the variation of wave heights over the year in location *e*. It shows the monthly average 95th percentile H_s from 1959 to 2021. For comparison, the 95th percentile H_s for the whole period is 2.28 m. The variation of wave heights in location *e* are representative of the seasonal pattern of wave heights along the entire study area, where the period from October to March has the greatest wave exposure. Specifically, November, December, and January, are the months with the highest wave heights. The months of April to September are characterized by smaller wave heights.

3.3. Interannual variability

Fig. 7 shows the distribution of annual wave energy concerning wave direction at location *e*; red colours indicate higher energy. Based on the monthly distribution of wave heights, the definition of the year was set from July to June, the proceeding calendar year, so that one consecutive winter season is represented. Summing the annual wave energy across the dominating sectors, east (0–180°) and west (180–360°), the west typically dominates over the east and dictates the shape of the total energy (Fig. 7b). Wave energy from the west sector on average accounts for 62% of the total annual energy. However, occasionally the annual energy in the east sector dominates over the west, for example, in years 1960, 1969, 1979, 1996, and 2003.

The results reveal an interannual variability of the wave conditions. It is possible to observe a distinct variation between the years in the hindcast series with respect to the quantity of wave energy and the dominating directions. The west-southwest is for most years the dominating wave direction, but eastern-directed events do occur. This corresponds to the statistics presented by the wave rose Fig. 5e, where the frequency of occurrence is less for waves in the eastern sector than the western sector.

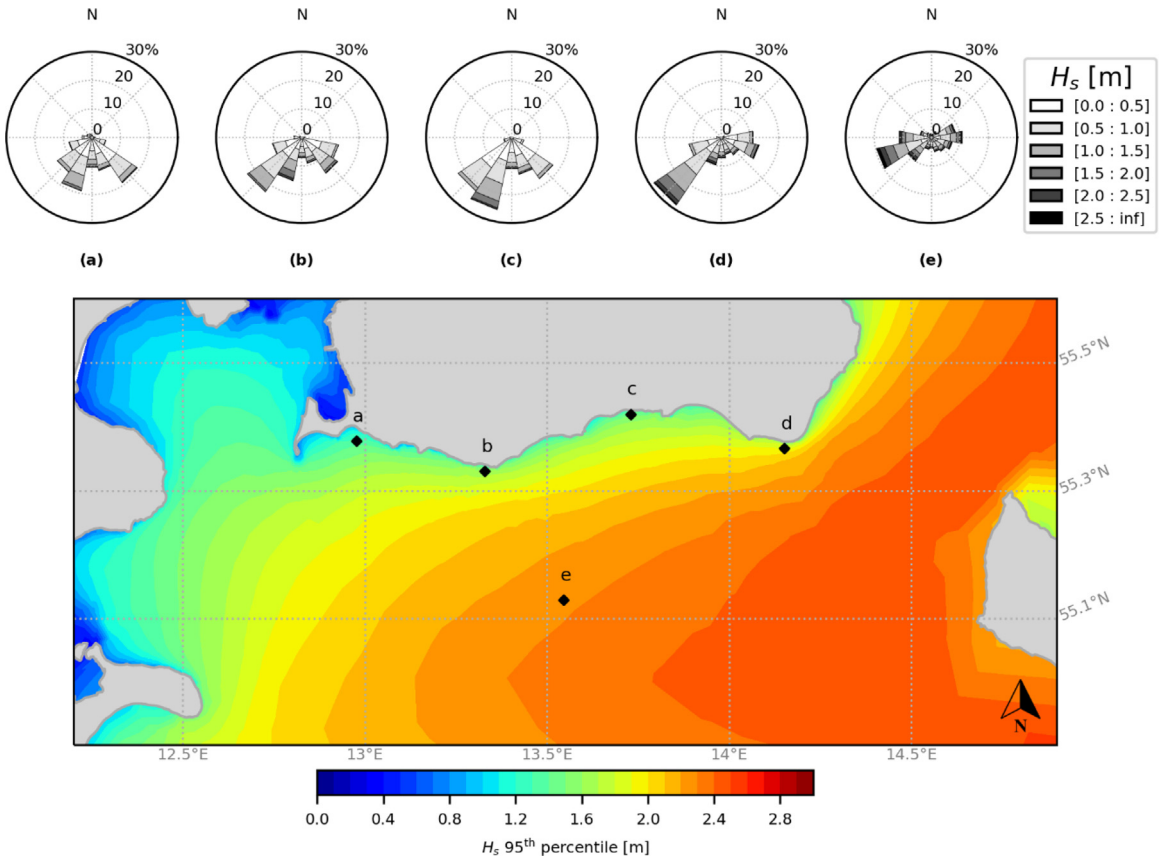

Fig. 5. Wave roses at four locations (10 m depth contour) along the Swedish south coast based on the years 1959–2021 (a-e). The map showcases the spatial distribution of 95th percentile H_s for the southwestern part of the basin.

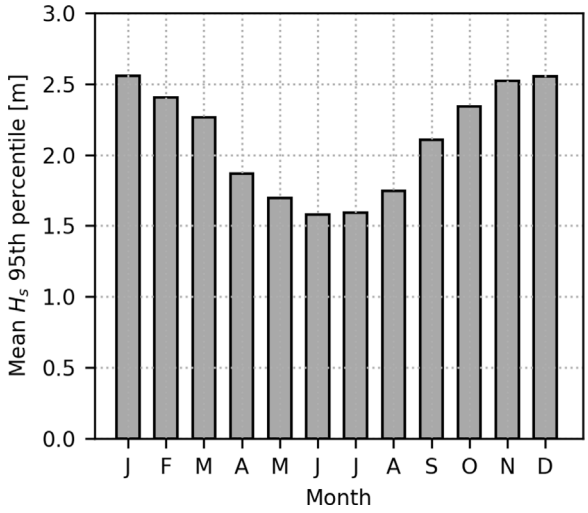

Fig. 6. Monthly distribution of 95th percentile H_s [m] for location *e*, based on data from 1959–2021.

3.4. Correlation to NAO

The oscillating behaviour observed in the wave energy analysis, characterized by altering west-easterly dominance, corresponds to the behaviour of the NAO. Fig. 8 displays the correlation between the NAO DJFM station-based index and annual energies from all directions and from the west and east sectors. For the total annual energy (Fig. 8a-b), the analysis yields a result for the Spearman correlation coefficient of 0.51, with a statistical significance of p<0.001. The annual energy in the western sector results in an even stronger correlation where the Spearman coefficient is 0.75 (Fig. 8c-d). On average, the annual westerly energy accounts for 62% of the total annual energy, and due to this dominance, the total annual energy is also positively correlated to the NAO index. As for the energy in the easterly sector, the correlation analysis gives a negative correlation to the NAO, with a Spearman correlation coefficient of −0.57 (Fig. 8e-f). The correlation coefficients reflect the behaviour of the oscillation where larger quantities of westerly energy are correlated with larger positive values of the NAO index. When the NAO is in the positive phase, the westerly winds are stronger. Whereas in the negative phase, the westerly winds are weaker, and easterly winds dominate instead. This is also reflected in the negative Spearman correlation coefficient obtained for the easterly sector. Subtracting the easterly energy from the westerly to obtain the net energy at location *e*, gives a dominating positive result as westerly directions dominate most annual wave fields. Years with negative net energy are observed in the series and these coincide with the negative phase of the NAO. The correlation of the annual net energy and the NAO index is positively correlated with a Spearman rank correlation coefficient of 0.74. There is spatial variation in the strength of correlation when comparing the offshore location *e* to the nearshore locations *a-d*. Spearman correlation coefficients for total annual energy compared to the NAO index are *a*: 0.63, *b*: 0.58, *c*: 0.64, and *d*: 0.56. The nearshore locations thus display a stronger positive correlation than the offshore location *e*.

4. Discussion

A 62-years hindcast wave data set from 1959–2021 was presented for the southern Baltic Sea with a focus on the south

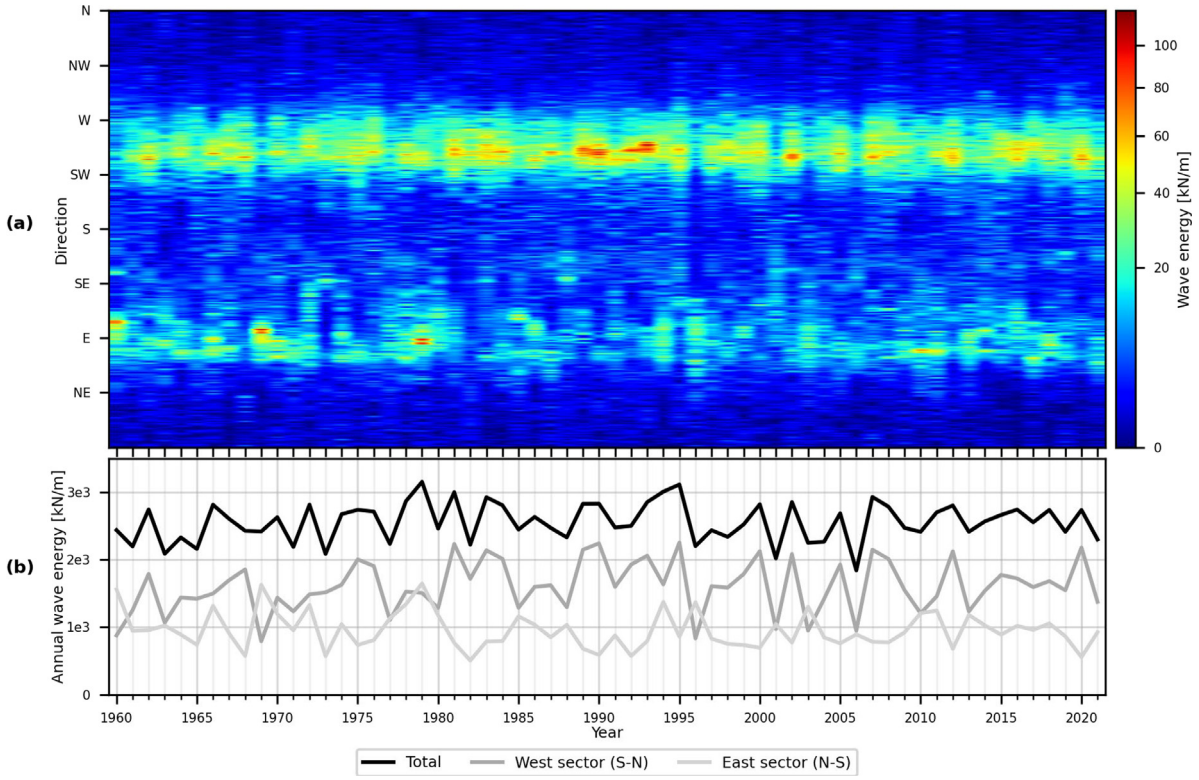

Fig. 7. Distribution of wave energy with respect to the incoming direction for offshore location *e* (a). Time series with annual wave energy 1959–2021 (b).

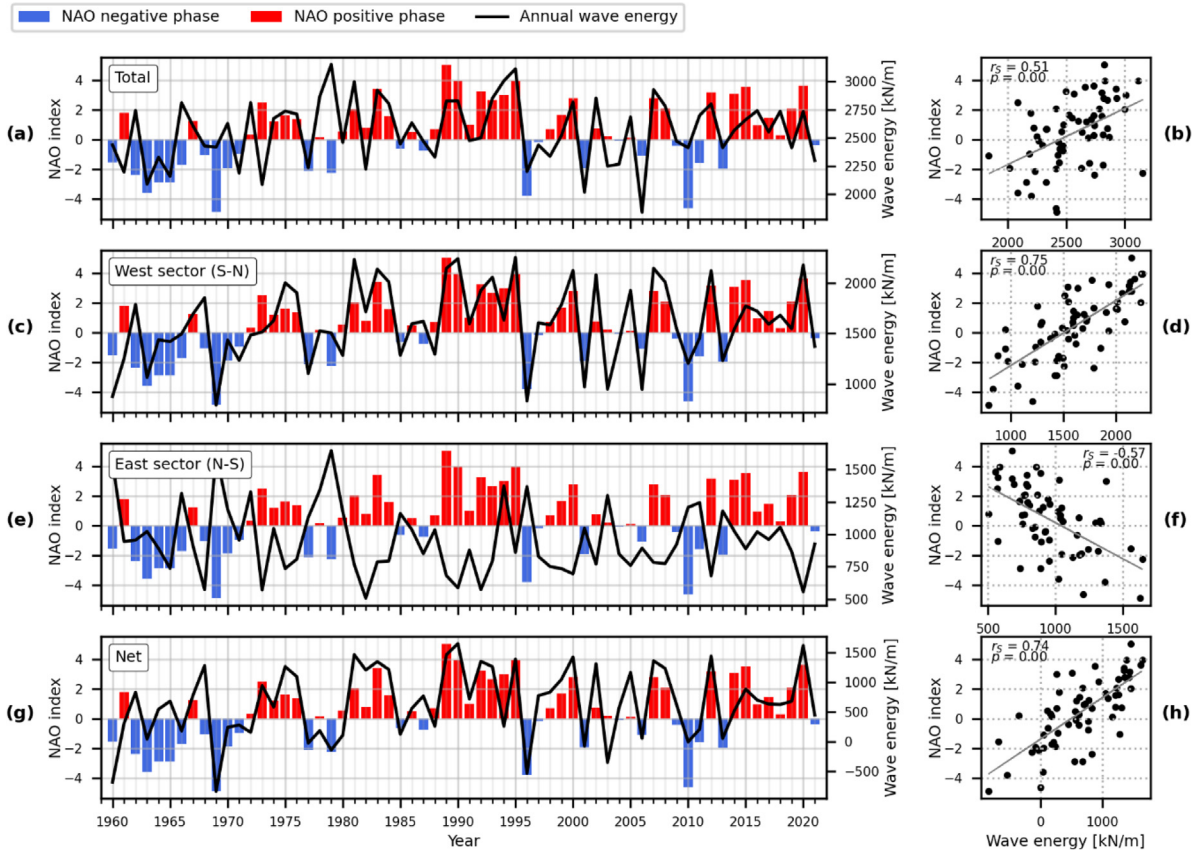

Fig. 8. Relationship between NAO DJFM station-based index and the annual wave energy during 1959–2021, with the corresponding Spearman rank correlation, for total annual energy (a-b), west energy (c-d), east energy (e-f) and net energy (west-east) (g-h).

coast of Sweden. The SWAN wave model described the multi-scale wave climate validated in both offshore basins and shallower nearshore coastal areas with a satisfactory performance when compared to observations. This implies that complete wave transformation from deeper water to shallow depths is well-represented in the model. Compared with other studies that present hindcast wave climate for the Arkona basin (Björkqvist et al., 2018; Blomgren et al., 2001; Soomere et al., 2012) the obtained model indicates a similar or improved performance.

The obtained average R^2-value of 0.83 for significant wave height indicates good model accuracy. However, average R^2 for wave period and direction are 0.53 and 0.68, respectively, which means that the model does not show as good accuracy for these parameters. This can partly be explained by the model discretization into 36 directional bins resulting in ten degree resolution for simulated θ, whereas the observations have a resolution of one degree. Another explanation is the measurement range of the surface acceleration buoys. Previous studies have pointed to the limitations associated with measuring short waves with surface acceleration buoys (Guimarães et al., 2018). When low-energy noise ($H_s/L < 0.012$) in the observed nearshore records was excluded, the fit of T_p and θ improved.

The model performance was improved mainly by calibrating the white capping coefficient in SWAN. Similar calibration methods have been reported from other studies using ERA5 reanalysis wind data to force SWAN (Beyramzade et al., 2019). Reliability assessment of ERA5 reanalysis wind has shown it is accurate for use in offshore and flat areas, while uncertainties in wind speed have been reported in coastal and mountainous areas (Gualtieri, 2021). Specifically for coastal locations, the land-sea discontinuity gives rise to differences in, e.g., surface roughness (Gualtieri, 2021). The resolution of ERA5 may not be adequate to reproduce this inconsistency in nearshore areas.

For wave modelling applications, it is known that the quality of wind fields applied to drive the model will govern the model results and hence the model performance (Soomere, 2022). The underestimation of the largest wave heights for the nearshore stations at Kämpinge and Ystad could be explained by the spatial resolution of the wind data. The ERA5 reanalysis applies an averaged representation of the local terrain, vegetation, and buildings that can give deviating results when reanalysis wind is compared to observations (Gualtieri, 2021). Overall, the evaluation of wave model results indicates a good fit compared to observations, but care should be taken in nearshore areas where the spatial resolution of the wind input may be insufficient to represent local effects.

The presented 62-year hindcast data series was analysed to characterize the temporal and spatial variability of the wave climate conditions in the southwestern Baltic Sea. Results highlight the influence of the basin characteristics on the local wave climate and hydrodynamic conditions. The shape of the coastline of south Sweden causes a spatial variation in wave height frequency and directional distribution.

The interannual wave climate is characterized by alternating west-eastern dominance in the wave conditions. Waves from the west sector, on average, accounts for 62% of the magnitude of the total annual wave energy but specific years with greater quantities of wave energy from the east sector occur. The correlation analyses of the annual wave energy and the NAO DJFM station-based index show that the NAO can explain the interannual variability for the quantity and direction of wave energy. The alternating positive and negative phases of the NAO are drivers for west-eastern directed energy and have implications for the resulting wave climate along the south coast of Sweden. The coastline is characterized by sandy beaches and eroding bluffs, interrupted by harbours and headlands. Thus, changes in the distribution of the incoming direction of wave energy can locally influence erosion and accretion processes along the coast. In this study we have established that interannual patterns in wave energy forcing in the southern Baltic Sea are governed by large-scale atmospheric circulation, NAO, and its variability. Coastlines in wave dominated environments respond to temporal changes in magnitude and direction of wave energy. Previous studies have established relationships between long-term shoreline change and the NAO, in e.g., France, Poland, and the United Kingdom (Masselink et al., 2023; Robinet et al., 2016; Rozyński and Szmytkiewicz, 2012; Thomas et al., 2010). Consequently, showing that climate indices can be used as a proxy for coastal evolution, in terms of periodic change in shoreline position and beach sediment volumes. These studies indicate the potential to include weather-regimes, rather than wave climate, as a driving force in shoreline evolution studies.

In addition to the NAO, other large-scale atmospheric systems govern climate conditions in the Baltic Sea region, e.g., Arctic Oscillation and the Scandinavian pattern. All these three indices have been considered in the study by Najafzadeh et al. (2021), who investigated the relationship between monthly climate indices and Baltic Sea wave climate with EOF-analysis. For the winter months, they found a statistically significant positive correlation for the NAO and AO and a negative correlation for SCAND. In our study, we considered only the NAO because the shifting positive and negative phases correspond to alternating west and east dominance in the wind direction, which implies that both phases give a signal in the wave climate relevant to the south coast of Sweden because of its east–west orientation. The AO's positive and negative phases coincide with the NAO's positive and negative phases because the two teleconnection patterns are closely related. Hence, similar behaviour to the correlation is expected when compared to wave energy in the southern Baltic. Regarding the Scandinavian pattern, the positive and negative phases are opposite to the NAO. In the negative phase of the SCAND, wind directions in the west to northwest dominate and positive phase east to southeast winds dominate. Since winds from the northwest are less relevant for the littoral processes on the south coast of Sweden, it was discarded in our analysis. The NAO index is available for period that extends further back in time compared to the ERA5 data (Fig. 9). The correlation between the wave energy and direction presented in this study could thus be used to analyse historical trends in wave energy regimes in the south Baltic Sea. The statistically significant correlations presented in our study highlight the importance of considering atmospheric circulation dynamics in deriving long-term magnitude and direction of wave climate conditions. Available projections of future wave field changes that include wave direction are lacking, although critical for risk assessments and effective coastal management (Morim et al., 2018).

5. Conclusions

This study presents a multi-decadal hindcast wave climate dataset for the southern Baltic Sea and nearshore wave observations from the south coast of Sweden. The model presents a detailed spatial resolution, particularly for the nearshore areas of south Sweden. With the same model configuration, satisfactory performance was obtained across the different spatial scales in the model.

Analysis of the wave climate data highlights the spatial and temporal variability in conditions in the south Baltic Sea basin. Intra-annual variation is characterized by more energetic conditions in the winter months compared to the summer. The interannual variability displays alternating east and west occurrence of wave energy, although westerly dominated energy

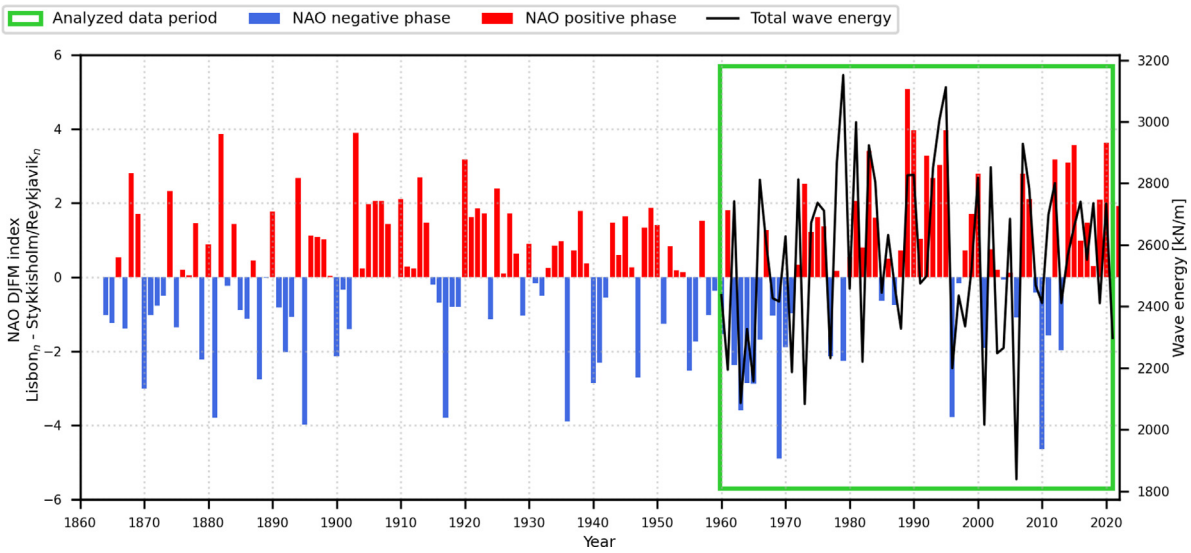

Fig. 9. NAO DJFM station-based index 1864–2022 plotted along with the extent of the analysed period with corresponding wave energy data.

prevails over east. Furthermore, the magnitude of annual wave energy displays a statistically significant positive correlation with the NAO DJFM station-based index. This is due to the predominance of strong westerly winds during the positive phase of the NAO.

CRediT authorship contribution statement

Anna Adell: Conceptualization, Formal analysis, Investigation, Methodology, Validation, Visualization, Writing – original draft, Writing – review & editing. **Björn Almström:** Conceptualization, Supervision, Writing – review & editing. **Aart Kroon:** Supervision, Writing – review & editing. **Magnus Larson:** Supervision, Writing – review & editing. **Cintia Bertacchi Uvo:** Conceptualization, Writing – review & editing. **Caroline Hallin:** Conceptualization, Project administration, Supervision, Writing – review & editing.

Declaration of competing interest

The authors declare that they have no known competing financial interests or personal relationships that could have appeared to influence the work reported in this paper.

Data availability

Data will be made available on request

Acknowledgements

This study was financed by the Swedish Transport Administration (grant number TRV 2019/96299). Simulations have been enabled through resources provided by LUNARC – Centre for Scientific and Technical Computing, Lund University. The authors would like to thank Almir Nunes de Brito Jr at Nioz for his valuable efforts and introduction to SWAN modelling. Thanks to Max Radermacher at Obscape for guidance and support regarding the measurement equipment and data processing. We want to thank Per-Jonas Qvist at Falsterbokanalens Båtklubb and Patrik Juhlin at Pdyk AB for assistance during the deployment and retirement of the wave buoys.

References

Andersson, H.C., 2002. Influence of long-term regional and large-scale atmospheric circulation on the baltic sea level. Tellus 54 (1), 76–88. http://dx.doi.org/10.1034/j.1600-0870.2002.00288.x.

Beyramzade, M., Mostafa, S., Majidy, M., 2019. Skill assessment of SWAN model in the red sea using different wind data. Reg. Stud. Mar. Sci. 30, 100714. http://dx.doi.org/10.1016/j.rsma.2019.100714.

Bierstedt, S.E., Hünicke, B., Zorita, E., 2015. Variability of wind direction statistics of mean and extreme wind events over the Baltic Sea region. Tellus 6 (1), http://dx.doi.org/10.3402/tellusa.v67.29073.

Björkqvist, J.V., Lukas, I., Alari, V., van Vledder, G.P., Hulst, S., Pettersson, H., Behrens, A., Männik, A., 2018. Comparing a 41-year model hindcast with decades of wave measurements from the Baltic Sea. Ocean Eng. 152 (2017), 57–71. http://dx.doi.org/10.1016/j.oceaneng.2018.01.048.

Blomgren, S., Larson, M., Hanson, H., 2001. Numerical modeling of the wave climate in the southern baltic sea. J. Coast. Res. 17 (2), 342–352.

Bonaduce, A., Staneva, J., Behrens, A., Bidlot, J.R., Wilcke, R.A.I., 2019. Wave climate change in the North Sea and Baltic Sea. J. Mar. Sci. Eng. 7 (6), http://dx.doi.org/10.3390/jmse7060166.

Booij, N., Ris, R.C., Holthuijsen, L.H., 1999. A third-generation wave model for coastal regions 1. Model description and validation. J. Geophys. Res.: Oceans 104 (C4), 7649–7666. http://dx.doi.org/10.1029/98JC02622.

Broman, B., Hammarklint, T., Rannat, K., Soomere, T., Valdmann, A., 2006. Trends and extremes of wave fields in the north-eastern part of the Baltic Proper. Oceanologia 48 (SUPPL.), 165–184.

BSH, 2019. FINO2 - Oceanographic Sensor Overview.

BSH, 2021. Sea state - Current measurements in North Sea and Baltic Sea. https://www.bsh.de/EN/DATA/Climate-and-Sea/Sea_state/sea_state_node.html.

Cavaleri, L., Alves, J.H.G.M., Ardhuin, F., Babanin, A., Banner, M., Belibassakis, K., Benoit, M., Donelan, M., Groeneweg, J., Herbers, T.H.C., Hwang, P., Janssen, P.A.E.M., Janssen, T., Lavrenov, I.V., Magne, R., Monbaliu, J., Onorato, M., Polnikov, V., Resio, D., et al., 2007. Wave modelling - the state of the art. Prog. Oceanogr. 75 (4), 603–674. http://dx.doi.org/10.1016/j.pocean.2007.05.005.

Davidson-Arnott, R., 2010. Introduction to Coastal Processes and Geomorphology. Cambridge University Press.

EMODnet, 2021. Emodnet bathymetry. https://www.emodnet-bathymetry.eu/.

Gualtieri, G., 2021. Reliability of ERA5 reanalysis data for wind resource assessment: A comparison against tall towers. Energies 14 (14), http://dx.doi.org/10.3390/en14144169.

Guimarães, P.V., Ardhuin, F., Sutherland, P., Accensi, M., Hamon, M., Perignon, Y., Thomson, J., Benetazzo, A., Ferrant, P., 2018. A surface kinematics buoy (SKIB) for wave–current interaction studies. Ocean Sci. 14 (6), 1449–1460.

Hersbach, H., Bell, B., Berrisford, P., Hirahara, S., Horányi, A., Muñoz-Sabater, J., Nicolas, J., Peubey, C., Radu, R., Schepers, D., Simmons, A., Soci, C., Abdalla, S., Abellan, X., Balsamo, G., Bechtold, P., Biavati, G., Bidlot, J., Bonavita, M., et al., 2020. The ERA5 global reanalysis. Q. J. R. Meteorol. Soc. 146 (730), 1999–2049. http://dx.doi.org/10.1002/qj.3803.

Holthuijsen, L.H., 2007. Waves in Oceanic and Coastal Waters. Cambridge University Press.

Huntley, D.A., 2013. Waves. In: Treatise on Geomorphology. Vol. 10, Elsevier Ltd, http://dx.doi.org/10.1016/B978-0-12-374739-6.00271-2.

Hurrell, J.W., 1995. Decadal trends in the north atlantic oscillation: Regional temperatures and precipitation. Science 269 (5224), 676–679.
Hurrell, J.W., Kushnir, Y., Ottersen, G., Visbeck, M., 2003. The North Atlantic Oscillation: Climate Significance and Environmental Impact. American Geophysical Union.
Jevrejeva, S., Moore, J.C., Grinsted, A., 2003. Influence of the Arctic Oscillation and El Niño-Southern Oscillation (ENSO) on ice conditions in the Baltic Sea: The wavelet approach. J. Geophys. Res.: Atmos. 108 (21), 1–11. http://dx.doi.org/10.1029/2003jd003417.
Jönsson, A., Broman, B., Rahm, L., 2003. Variations in the Baltic Sea wave fields. Ocean Eng. 30 (1), 107–126. http://dx.doi.org/10.1016/S0029-8018(01)00103-2.
Komen, G.J., Hasselmann, S., Hasselmann, K., 1984. On the existence of a fully developed wind-sea spectrum. J. Phys. Oceanogr. 14 (8), 1271–1285. http://dx.doi.org/10.1175/1520-0485(1984)014%3C1271:OTEOAF%3E2.0.CO;2.
Larson, M., Fredriksson, C., Hanson, H., 2016. Changing wind properties in south Sweden since the days of Tycho Brahe. VATTEN - J. Water Manag. Res. 1, 117–128.
Larson, M., Hanson, H., 1993. Erosion along the coast of south Sweden. In: Proceedings of the Hiltonhead Island International Coastal Symposium. pp. 92–98.
Leppäranta, M., Myrberg, K., 2009. Physical oceanography of the baltic sea. In: Paper Knowledge. Toward a Media History of Documents.
Lincke, D., Hinkel, J., 2018. Economically robust protection against 21st century sea-level rise. Global Environ. Change 51 (2017), 67–73. http://dx.doi.org/10.1016/j.gloenvcha.2018.05.003.
Luijendijk, A., Hagenaars, G., Ranasinghe, R., Baart, F., Donchyts, G., Aarninkhof, S., 2018. The state of the world's beaches. Sci. Rep. 8 (1), 1–11. http://dx.doi.org/10.1038/s41598-018-24630-6.
Malmberg-Persson, K., Nyberg, J., Ising, J., Rodhe, L., 2016. Skånes känsliga stränder – erosionsförhållanden och geologi för samhällsplanering. SGU-report 2016, 17.
Masselink, G., Scott, T., Poate, T., Stokes, C., Wiggins, Ma, Valiente, N., Konstantinou, A., 2023. Tale of two beaches: correlation between decadal beach dynamics and climate indices. Coast. Sediment. 2023, http://dx.doi.org/10.1142/9789811275135_0031.
Morim, J., Hemer, M., Cartwright, N., Strauss, D., Andutta, F., 2018. On the concordance of 21st century wind-wave climate projections. Glob. Planet. Change 167 (May), 160–171. http://dx.doi.org/10.1016/j.gloplacha.2018.05.005.
Najafzadeh, F., Kudryavtseva, N., Soomere, T., 2021. Effects of large-scale atmospheric circulation on the Baltic Sea wave climate: application of the EOF method on multi-mission satellite altimetry data. Clim. Dynam. 57 (11–12), 3465–3478. http://dx.doi.org/10.1007/s00382-021-05874-x.
NCAR, 2023. Hurrell north atlantic oscillation (NAO) index (station-based). https://climatedataguide.ucar.edu/climate-data/hurrell-north-atlantic-oscillation-nao-index-station-based.
Nicholls, R.J., 2002. Analysis of global impacts of sea-level rise: A case study of flooding. Phys. Chem. Earth 27 (32–34), 1455–1466. http://dx.doi.org/10.1016/S1474-7065(02)00090-6.
Obscape, B.V., WaveDroid Block III C Manual Revision 2.
Omstedt, A., Chen, D., 2001. Influence of atmospheric circulation on the maximum ice extent in the Baltic Sea. J. Geophys. Res.: Oceans 106 (C3), 4493–4500. http://dx.doi.org/10.1029/1999jc000173.
Oppenheimer, M., Glavovic, B.C., Hinkel, J., van de Wal, R., Magnan, A.K., Abd-Elgawad, A., Cai, R., Cifuentes-Jara, M., DeConto, R.M., Ghosh, T., Hay, J., Isla, F., Marzeion, B., Meyssignac, B., Sebesvari, Z., 2019. In: Pörtner, H.-O., Roberts, D.C., Masson-Delmotte, V., Zhai, P., Tignor, M., Poloczanska, E., Mintenbeck, K., Alegría, A., Nicolai, M., Okem, A., Petzold, J., Rama, B. (Eds.), Sea Level Rise and Implications for Low-Lying Islands, Coasts and Communities Coordinating. N. M. W. IPCC Special Report on the Ocean and Cryosphere in a Changing Climate.
Pettersson, H., Lindow, H., Brüning, T., 2014. Wave climate in the baltic sea in 2013. In: HELCOM Baltic Sea Environment Fact Sheets. http://www.helcom.fi/baltic-sea-trends/environment-fact-sheets/.
Roberts, K.J., Pringle, W.J., Westerink, J.J., 2019. OceanMesh2D 1.0: MATLAB-based software for two-dimensional unstructured mesh generation in coastal ocean modeling. Geosci. Model Dev. 12 (5), 1847–1868. http://dx.doi.org/10.5194/gmd-12-1847-2019.
Robinet, A., Castelle, B., Idier, D., Le Cozannet, G., Déqué, M., Charles, E., 2016. Statistical modeling of interannual shoreline change driven by North Atlantic climate variability spanning 2000–2014 in the Bay of Biscay. Geo-Mar. Lett. 36 (6), 479–490. http://dx.doi.org/10.1007/s00367-016-0460-8.
Rosentau, A., Bennike, O., Uscinowicz, S., Miotk-Szpiganowicz, G., 2017. The baltic sea basin. In: Submerged Landscapes of the European Continental Shelf: Quaternary Paleoenvironments (Issue May). http://dx.doi.org/10.1002/9781118927823.ch5.
Rozyński, G., Szmytkiewicz, P., 2012. Long term evolution of baltic sea sandy beach forced by winter north atlantic oscillation (NAOWI). In: Proceedings of the Coastal Engineering Conference. pp. 1–10. http://dx.doi.org/10.9753/icce.v33.sediment.70.
Rutgersson, A., Jaagus, J., Schenk, F., Stendel, M., 2014. Observed changes and variability of atmospheric parameters in the Baltic Sea region during the last 200 years. Clim. Res. 61 (2), 177–190. http://dx.doi.org/10.3354/cr01244.
SMHI, 2022. Vågbojar. https://smhi.se/kunskapsbanken/oceanografi/oceanografiska-matningar/vagbojar-1.180392.
Soomere, T., 2022. Numerical simulations of wave climate in the Baltic Sea: a review. Oceanologia http://dx.doi.org/10.1016/j.oceano.2022.01.004, xxxx.
Soomere, T., Räämet, A., 2011. Spatial patterns of the wave climate in the Baltic Proper and the Gulf of Finland. Oceanologia 53 (1-TI), 335–371. http://dx.doi.org/10.5697/oc.53-1-TI.335.
Soomere, T., Weisse, R., Behrens, A., 2012. Wave climate in the Arkona Basin, the Baltic Sea. Ocean Sci. 8 (2), 287–300. http://dx.doi.org/10.5194/os-8-287-2012.
Suursaar, U., Tõnisson, H., Alari, V., Raudsepp, U., Rästas, H., Anderson, A., 2016. Projected changes in wave conditions in the baltic sea by the end of 21st century and the corresponding shoreline changes. J. Coast. Res. 1 (75), 1012–1016. http://dx.doi.org/10.2112/SI75-203.1.
Svensson, J., Wickström, K., 1986. Vågdata från svenska kustvatten 1986, Nr221987.
The SWAN Team, 2020. USER MANUAL SWAN - cycle III version 41.31a.
Thomas, T., Phillips, M.R., Williams, A.T., 2010. Mesoscale evolution of a headland bay: Beach rotation processes. Geomorphology 123 (1–2), 129–141. http://dx.doi.org/10.1016/j.geomorph.2010.06.018.
USACE, 1984. Shore Protection Manual. Government Printing Office.
Van der Meer, J.W., Allsop, N.W.H., Bruce, T., De Rouck, J., Kortenhaus, A., Pullen, T., Schüttrumpf, H., Troch, P., Zanuttigh, B., 2018. EurOtop - manual on wave overtopping of sea defences and related structures. https://www.overtopping-manual.com.
Wong, P.P., Losada, I.J., Gattuso, J.-P., Hinkel, J., Khattabi, A., McInnes, K.L., Saito, Y., Sallenger, A., 2014. Coastal systems and low-lying areas. In: Field, C., Barros, V.R., Dokken, D.J., Mach, K.J., Mastrandrea, M.D., Bilir, T.E., Chatterjee, M., Ebi, K.L., Estrada, Y.O., Genova, R.C., Girma, B., Kissel, E.S., Levy, A.N., MacCracken, S., Mastrandrea, P.R., White, L.L. (Eds.), Climate Change 2014: Impacts, Adaptation, and Vulnerability. Part a: Global and Sectoral Aspects. Contribution of Working Group II To the Fifth Assessment Report of the Intergovernmental Panel on Climate Change. Cambridge University Press, pp. 361–409.
Woolf, D.K., Shaw, A.G.P., Tsimplis, M.N., 2003. The influence of the North Atlantic Oscillation on sea-level variability in the North Atlantic region. Glob. Atmosphere Ocean Syst. 9 (4), 145–167. http://dx.doi.org/10.1080/10236730310001633803.
Zijlema, M., 2009. Multiscale simulations using unstructured mesh swan model for wave. Coast. Dyn. 2, 1–12. http://dx.doi.org/10.1142/9789814282475.
Zijlema, M., 2010. Computation of wind-wave spectra in coastal waters with SWAN on unstructured grids. Coast. Eng. 57 (3), 267–277. http://dx.doi.org/10.1016/j.coastaleng.2009.10.011.